# Nature of the structural symmetries associated with hybrid improper ferroelectricity in $Ca_3X_2O_7$ ($X$ = Mn and Ti)

S. Liu,[1] H. Zhang,[1] S. Ghose,[2,*] M. Balasubramanian,[3] Zhenxian Liu,[4] S. G. Wang,[5] Y.-S. Chen,[5] B. Gao,[6,7] Jaewook Kim,[6,7] S.-W. Cheong,[6,7] and T. A. Tyson[1,7,†]

[1]*Department of Physics, New Jersey Institute of Technology, Newark, New Jersey 07102, USA*
[2]*National Synchrotron Light Source II, Brookhaven National Laboratory, Upton, New York 11973, USA*
[3]*Advanced Photon Source, Argonne National Laboratory, Argonne, Illinois 60439, USA*
[4]*Department of Physics, University of Illinois at Chicago, Illinois 60607-7059, USA*
[5]*Center for Advanced Radiation Sources, University of Chicago, Argonne, Illinois 60439, USA*
[6]*Department of Physics and Astronomy, Rutgers University, Piscataway, New Jersey 08854, USA*
[7]*Rutgers Center for Emergent Materials, Rutgers University, Piscataway, New Jersey 08854, USA*

(Received 18 March 2019; revised manuscript received 15 May 2019; published 27 June 2019)

In hybrid improper ferroelectric systems, polarization arises from the onset of successive nonpolar lattice modes. In this work, measurements and modeling were performed to determine the spatial symmetries of the phases involved in the transitions to these modes. Structural and optical measurements reveal that the tilt and rotation distortions of the $MnO_6$ or $TiO_6$ polyhedra relative to the high symmetry phases driving ferroelectricity in the hybrid improper $Ca_3X_2O_7$ system ($X$ = Mn and Ti) condense at different temperatures. The tilt angle vanishes abruptly at $T_T \sim 400$ K for $Ca_3Mn_2O_7$ (and continuously for $X$ = Ti) and the rotation mode amplitude is suppressed at much higher temperatures $T_R \sim 1060$ K. Moreover, Raman measurements in $Ca_3Mn_2O_7$ under isotropic pressure reveal that the polyhedral tilts can be suppressed by very low pressures (between 1.4 and 2.3 GPa) indicating their softness. These results indicate that the $Ca_3Mn_2O_7$ system provides a platform for strain engineering of ferroelectric properties in film-based systems with substrate-induced strain.

DOI: 10.1103/PhysRevB.99.224105

## I. INTRODUCTION

A broad range of mechanisms is known to produce ferroelectricity in solid materials including intrinsically atomic effects such as lone pairs (e.g., $6s^2$ in $BiFeO_3$ [1]) or ion size mismatch leading to off-center lattice distortions in the classical $BaTiO_3$ system [2–4]. From a microscopic perspective, these materials fall into two main classes having net electric polarization due to atomic displacement, such as the $ABO_3$ system, where an off-center $B$ atom displacement is proposed. Alternatively, order-disorder transitions have also been proposed in these systems. In general, the microscopic mechanisms driving ferroelectric behavior are thought to cause a $\Gamma$ point instability in the ordering of a polar mode of the parent structure. There is a direct connection between the polarization amplitude and the structural polar mode.

Distinct from these mechanisms above are a class of improper ferroelectrics in which the polarization is a secondary order parameter. Recently, the layered perovskites ($n = 2$ Ruddelsen-Popper structure with double stacked $MnO_6$ polyhedra, $A_3B_2O_7$) was predicted to support ferroelectrics induced by the introduction of a rotation pattern due to two independent nonpolar rotations of the $BO_6$ polyhedra [5] relative to the high symmetry $I4/mmm$ (#139) phase at high temperature. The structure is characterized by an $X_2^+$ rotation of the $MnO_6$ polyhedra in the high symmetry plane and a $X_3^-$ tilt relative to the high symmetry (long) axis. The polarized state of this system is determined by the combined rotation and tilt structural modes. In these hybrid improper ferroelectrics, density functional theory (DFT) calculations reveal that the symmetry of the phase exhibiting ferroelectricity has space group $A2_1am$ (#36, $Cmc2_1$ in standard setting). The rotations couple directly with the magnetic order of the Mn sites (having $G$-type antiferromagnetic order) at low temerature [6].

The nature of the transition from the high-temperature $I4/mmm$ phase to the low-temperature $A2_1am$ phase is not well understood. Determination of whether the rotation and tilt structural changes onset collectively or separately, the nature of the transitions (first or second order), and the appropriate long range and local symmetries present is essential to the development of accurate theoretical models. Limited structural powder diffraction work suggests that the $Ca_3Mn_2O_7$ system undergoes a transition into an intermediate $Acaa$ phase (#68, $Ccca$ standard setting) [7]. In polycrystalline samples, the proximity of the $Acaa$ and $A2_1am$ phase in energy was found to produce a broad mixed phase region. Additional symmetry possibilities of the intermediate state include the $Acam$, $Amam$, and $F2mm$ space groups. While clear switchable ferroelectric polarization has been observed in Ti and Sn-based systems ($B$ site), the manganese perovskite system has not been seen to exhibit this critical behavior needed for device applications. A complex domain structure with the stacking of $a$ and $b$ domains along the $c$ axis (long axis) has been found to suppress polarization in $Ca_3Mn_2O_7$ [8]. The primary difference between $Ca_3Mn_2O_7$ (with the coupling of magnetic

*Corresponding author: sghose@bnl.gov
†Corresponding author: tyson@njit.edu

 ©2019 American Physical Society

order and structure but no finite electric polarization) and the $Ca_3Ti_2O_7$ (with large electric polarization, 8 $\mu C/cm^2$) [9] is the stability of $A2_1am$ low-temperature phase in the Ti-based system over a broad range of temperatures and its switchable room temperature electric polarization.

Systematic studies of the $Ca_3Mn_{2-x}Ti_xO_7$ mixed system have been initiated to understand the electric polarization domain structure and magnetic order in this system [7]. Recent Raman measurements up to 350 K on single crystals of $Ca_3Mn_2O_7$ indicate a significant softening of a mode near 107 $cm^{-1}$ which was assigned to be an antiphase tilting mode bases on phonon calculations utilizing classical interaction potentials [10]. Shifts in the modes corresponding to tilting and rotation were examined, and it is argued that reduction of the frequency of the tilting mode with temperature indicates that this is a transition from $Cmc2_1$ ($A2_1am$) to an assumed $Ccca$ ($Acaa$) intermediate phase is driven by a tilt rotation. An intermediate phase region with the coexistence of competing soft modes with distinct phases was found to be consistent with these measurements. However, no direct structural information was presented.

Neutron diffraction and laboratory-based x-ray diffraction structural measurements on the $B$ site (Ti or Mn)-doped system $Ca_3Mn_{0.9}Ti_{0.1}O_7$ found antiphase tilting of the $MnO_6$ polyhedra decreases in amplitude while the rotation remains unchanged with increasing temperature and pressure [11]. The tilting was found to decrease smoothly (from ~8° to ~6.5°), going from ~10 to ~375 K, with a kink near the magnetic ordering temperature $T_N$. In the analysis in that work, the single-crystal neutron scattering measurements reveal a polar $Aba2$ space group at 450 K. It was indicated that $Ca_3Ti_2O_7$, by contrast, would have enhancement of both antiphase tilt and in-plane distortion with increasing temperature.

To fully understand the nature of the transitions in this material, structural measurements on the endmember $Ca_3Mn_2O_7$ and $Ca_{2.4}Sr_{0.6}Ti_2O_7$ (representing $CaTiO_3$) were conducted over a broad temperature range. Samples derived from single crystals were used in all measurements. Heat capacity (2 to 380 K) and differential scanning calorimetry [DSC, 300 to 500 K] measurements were conducted. Local structural pair distribution function (PDF) measurements were conducted between 100 and 1100 K at the NSLS II XPD (28-ID-2) Beamline and APS beamline 6-ID-D. X-ray absorption fine structure (XAFS) measurements were conducted with respect to the Mn site for the temperature range 300 and 1100 K (at beamline 8-ID at NSLS II), and with respect to the Ca site (at APS beamline 20 BM-B for temperatures near the ~400 K transition). Ti XAFS spectra were collected at NSLS2 beamline 8-ID between 300 and 650 K. High-resolution synchrotron single crystal diffraction measurements were conducted between 100 and 480 K (at APS beamline 15-ID-D). High-pressure Raman measurements were conducted at NSLS2 beamline 22-IR-1 to follow the changes in symmetry with pressure and determine the pressure ranges for the phase changes. Experimental and computation details including phonon mode information, Raman spectra, heat capacity, and differential scanning calorimetry (DSC) measurements, XAFS measurements and single crystal diffraction structural data (at 104, 300, and 480 K) are provided in the Supplemental Material [12].

Calorimetry measurements [DSC and heat capacity] reveal a second order transition near 110 K corresponding to the antiferromagnetic ordering temperature and a first-order transition near 367 K on cooling and near 405 K on warming in $Ca_3Mn_2O_7$. This first order transition is found in structural measurements corresponding to a loss of tilt angle (vanishing of $X_3^-$ tilt amplitude) above this transition on warming and yields an nonpolar space group ($I4/mmm$ or $C2/m$ with split in-plane oxygen sites). The transiton temperature is termed $T_T$. Distinct domains with the same space group are found. These measurements are supported by Raman observations. Local structural measurements reveal an enhanced Ca-Mn bond on warming above $T_T$ consistent with loss of electric polarization. No evidence of phase coexistence is found in $Ca_3Mn_2O_7$ near $T_T$. In this temperature region, thermal measurements reveal no clear phase transitions in polycrystalline samples. PDF and XAFS measurements reveal a transition near 1060 K consistent with the loss of the $X_2^+$ rotation amplitude (termed $T_R$).

Structural and spectroscopic measurements, conducted on the corresponding Ti-based system $Ca_{3-x}Sr_xTi_2O_7$ ($Ca_{2.4}Sr_{0.6}Ti_2O_7$), reveal the same trend. However, the loss of the $X_3^-$ tilt amplitude is found to be a continuous transition. DFT calculations on $Ca_3Mn_2O_7$ indicate that the relevant self force constant for the O sites are significantly softer for a local tilt distortion compared to local twist or rotational local distortion, consistent with the measurements. The phonon densitiy of states of both systems (containing Ti or Mn) are qualitatively similar. The overview of the general $Ca_3X_2O_7$ system is that near $T_T$ (~400 K) the tilt mode vanishes, while the rotational mode amplitude decrease continuously with increased temperature. High-pressure Raman measurements indicate loss of the tilt angle for very low pressures (between 1.4 and 2.3 GPa) revealing the softness of the tilt mode. Preparing thin film samples with substrate strain values near this critical crossover value in strain (near the ferro/paraelectric transition) will enable switching of polarization (on/off) using a piezoelectric substrate. The results also suggest that enhancement of the $A$-O bond strength will lift the temperature $T_T$ at which the polarization vanishes. Work on the $X$ = Mn system is presented in the main text and the $X$ = Ti system results are included in the Supplemental Material.

## II. QUALITATIVE STRUCTURE, PREDICTED PHONON SPECTRA, AND RAMAN MEASUREMENTS

Figure 1(a) shows the crystal structure of $Ca_3Mn_2O_7$ with respect to the $Cmc2_1$ space group (#36, standard setting) with the long axis along $a$. Note that there are three distinct types of O sites in this $n = 2$ Ruddlesden-Popper perovskite system. There are apical O sites bonded only to one Mn site and weakly bonded to the Ca sites, apical interior sites shared by two Mn sites along the $a$ axis, and planar O sites shared between two Mn site in the $b$-$c$ plane. Figure 1(b) shows the $MnO_6$ polyhedral rotation about the long axis ($X_2^+$, black curved arrow) and the tilts ($X_3^-$, blue arrows) of the polyhedra about an axis normal to the long axis.

Calculation of the force constants by DFT methods enables computation of the phonon density of states. Figure 1(c) shows the phonon density of states (DOS) projected onto

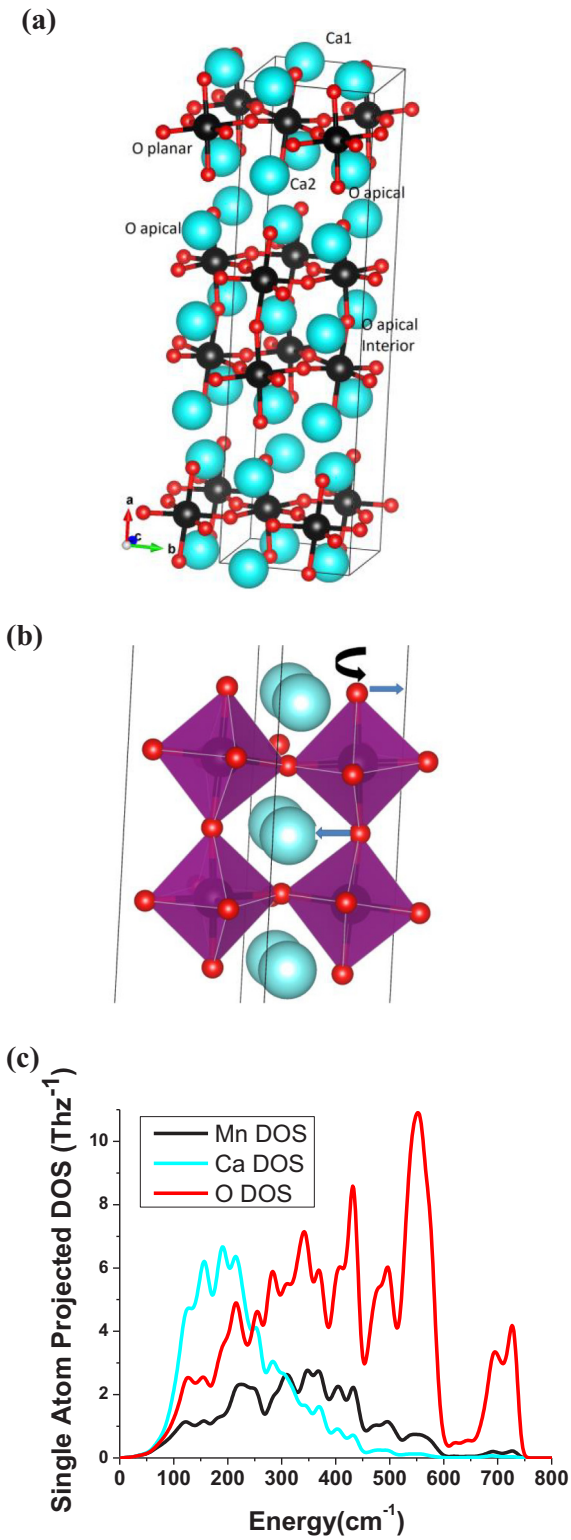


FIG. 1. (a) Low-temperature unit cell indicating unique O sites and (b) the $MnO_6$ polyhedral rotations about the long axis ($X_2^+$, black curved arrow) and the tilts ($X_3^-$, blue arrows) of the polyhedra normal to the long axis. (c) Partial phonon density of states derived from DFT simulations showing the Mn, Ca, and O site projected components. Note that the phonon DOS corresponding to the Ca sites vanishes for energies above ~450 $cm^{-1}$.

the Mn, Ca, and O sites separately. What can be seen is that although the Ca atoms are lower in mass than the Mn atoms, the main contribution to the phonon DOS at low energy (~100–300 $cm^{-1}$) is from the Ca sites. The Mn contributions are broad and extend up to ~600 $cm^{-1}$, while the O DOS covers the full energy range. Hence Ca atom motions dominate the low-frequency phonon modes while oxygen contributes at all frequencies. The similarity of the force constants indicates similar phonon DOS for $Ca_3Mn_2O_7$ and $Ca_3Ti_2O_7$. Indeed theoretical work on $Ca_3Ti_2O_7$ yield qualitatively similar phonon DOS [13] to that presented in Fig. 1(c).

Raman measurements were conducted on single crystal, and polycrystalline samples for temperatures between 100 and 500 K, covering the high end of any possible low-temperature transitions. In Fig. 2(a) we show spectra for the incident laser beam normal to the long axis ($x$ axis). Note the abrupt change in frequency in the peak near 615 $cm^{-1}$ on cooling below ~370 K (breathing mode of $MnO_6$ polyhedra, see below). Near the same temperature, the peak near 460 $cm^{-1}$ also vanishes. We note that a weak low-frequency peak near 146 $cm^{-1}$ in the spectrum is found to vanish with increasing temperature [see arrow in Fig. 2(a)]. The area of this peak vs temperature given in Fig. 2(b), indicates the abrupt dropoff with temperature. For the same measurement geometry, the peak position of the main peak near 615 $cm^{-1}$ is shown on warming and cooling in Fig. 2(c) and in Fig. S4(b). The abrupt transition is characteristic of first-order behavior. Measurement of a polycrystalline sample over the same temperature range reveals no step change, consistent with earlier measurements [7] on the same type of material suggesting mixed phase behavior. Figure S1 (Supplemental Material) shows the calculated displacement modes from DFT for phonons near 129 and 144 $cm^{-1}$ [Fig. S1(a), Fig. S1(b), and Table S1]. The lowest energy mode (126 $cm^{-1}$) corresponds to the shear motion of the Ca ion near the apical O atoms, while the calculated mode at 144 $cm^{-1}$ corresponds to the combined planar motion of the Ca sites and tilt rotations of the $MnO_6$ polyhedra. For both modes, all Ca atomic motions are in the $yz$ plane containing the electric polarization vector. The main peak at 612 $cm^{-1}$ [Fig. S1(c)] is characterized by a breathing mode of the $MnO_6$ polyhedra. The full set of calculated phonon frequencies at the Γ point are given in Table S1. The corresponding Raman spectra in an offset configuration for the laser beam normal to and along the long axis are given in Fig. S2. The measurements for the beam along the symmetry axis show suppression of the peak near 120 $cm^{-1}$ with increasing temperature (Fig S3, and additional surface plots in Fig. S4).

## III. CALORIMETRIC MEASUREMENTS

Heat capacity and DSC measurements on crystals of $Ca_3Mn_2O_7$ were used to identify the nature of the observed transitions. Low-temperature heat capacity measurements (Fig. S5) on both warming and cooling reveal a smooth transition near 110 K corresponding to the magnetic ordering temperature ($T_N$). The absence of hysteresis and the step-like shape indicates that the transition is second order. DSC

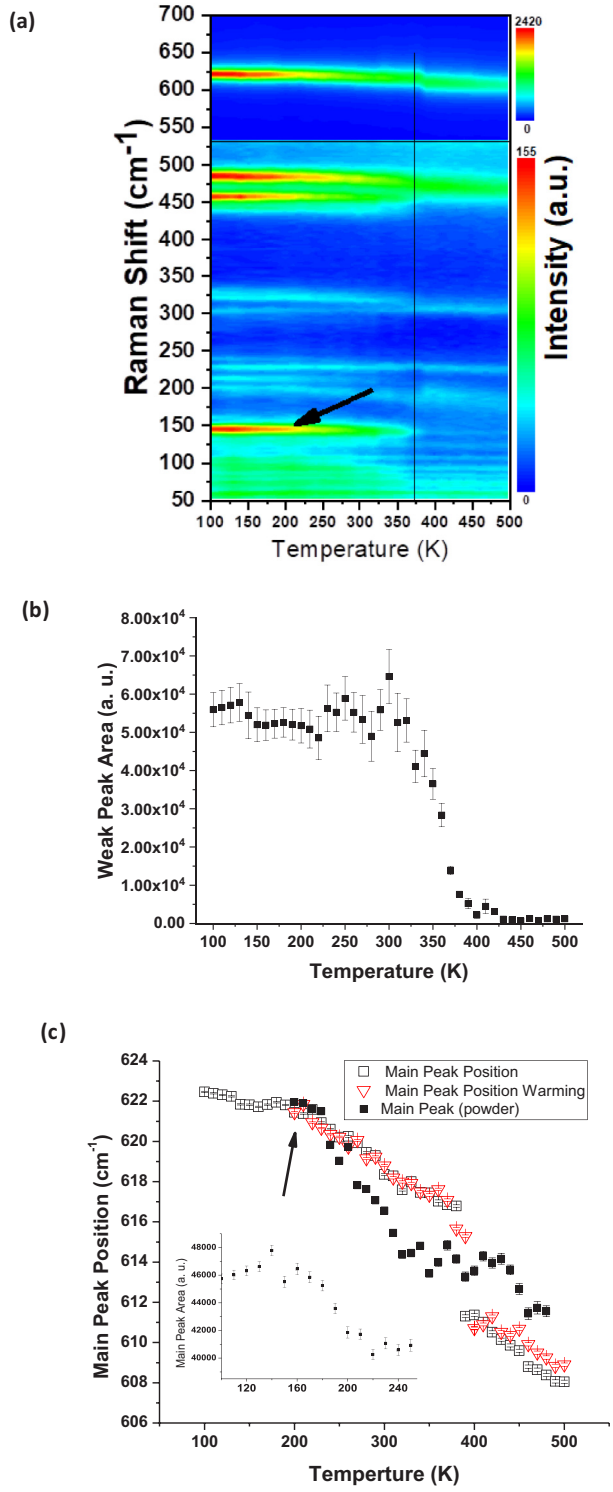


FIG. 2. (a) Raman spectra of a single crystal for photon beam normal to the long axis for data taken between 100 and 500 K. Note that the weak peak near ∼146 $cm^{-1}$ vanishes as temperature increases (measured on cooling from 500 K). The vertical line indicates the abrupt change in structure near 370 K (b) The weak peak [arrow in (a)] area vs. temperature is displayed showing that it disappears above ∼370 K. (c) comparison of the peak position vs. temperature for the main Raman peak for powder and single crystal samples. Data are for cooling unless both warming and cooling results are shown.

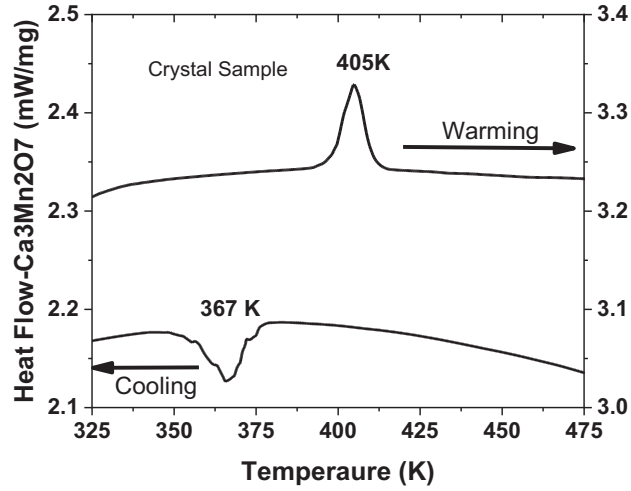


FIG. 3. DSC curves for $Ca_3Mn_2O_7$ (cooling rate = 20 K/min) from single crystal materials. Multiple scans reveal the high reproducibility of the transitions in both systems. The hysteresis in the complete loops (the transitions here at 405 K on warming and 367 K on cooling) reveal that the transition in $Ca_3Mn_2O_7$ is first order.

measurements on crystals at higher temperature (Fig. 3) reveal an abrupt structural transition at 405 K on warming and at 367 K on cooling the sample. This hysteresis indicates that the transition is first order in nature. No transition features are seen in the corresponding polycrystalline sample measurements [derived from the solid state reaction, Fig. S6(a)].

DSC measurements for $Ca_{2.4}Sr_{0.6}Ti_2O_7$ (from crystal samples having Sr for stability) indicate a very weak feature with the characteristic step change observed for continuous or glass-like transitions [Fig. S6(b)]. Raman measurements on single crystal $Ca_{2.4}Sr_{0.6}Ti_2O_7$ between 100 and 500 K (Figs. S7 and S8) indicate that low-frequency phonons near 93 and 112 $cm^{-1}$ soften smoothly with temperature indicating a continuous transition. Similar behavior is seen in polycrystalline samples of $Ca_3Ti_2O_7$ with low-frequency phonons near 121 $cm^{-1}$ (Figs. S9 and S10). The combined results indicate that the transition at $T_T$ is first order for the $X$ = Mn system and continuous for the $X$ = Ti system.

## IV. LOCAL STRUCTURAL MEASUREMENTS (X-RAY ABSORPTION SPECTROSCOPY)

Detailed structural measurements on $Ca_3Mn_2O_7$ were conducted to determine the changes in local and long-range structure with temperature. XAFS measurements relative to the Mn site were used to determine the changes in local structure between 300 and 1100 K (Fig. 4). Fits were made for Mn-O, Mn-Ca and Mn-Mn bond (covering the range up to ∼4 Å, Fig. S11). At high temperatures [Figs. 5(a) and 5(b)] the Mn-O and Mn-Ca bonds exhibit changes associated with ordering of the structure (near $T_R$). Examination of the structure function over the full temperature range reveals stiff Mn-O bonds and stiff Mn-Mn correlation with weak changes in the peak amplitudes with temperature (see Fig. S11) as predicted by the DFT simulations (Table I). The largest changes with temperature

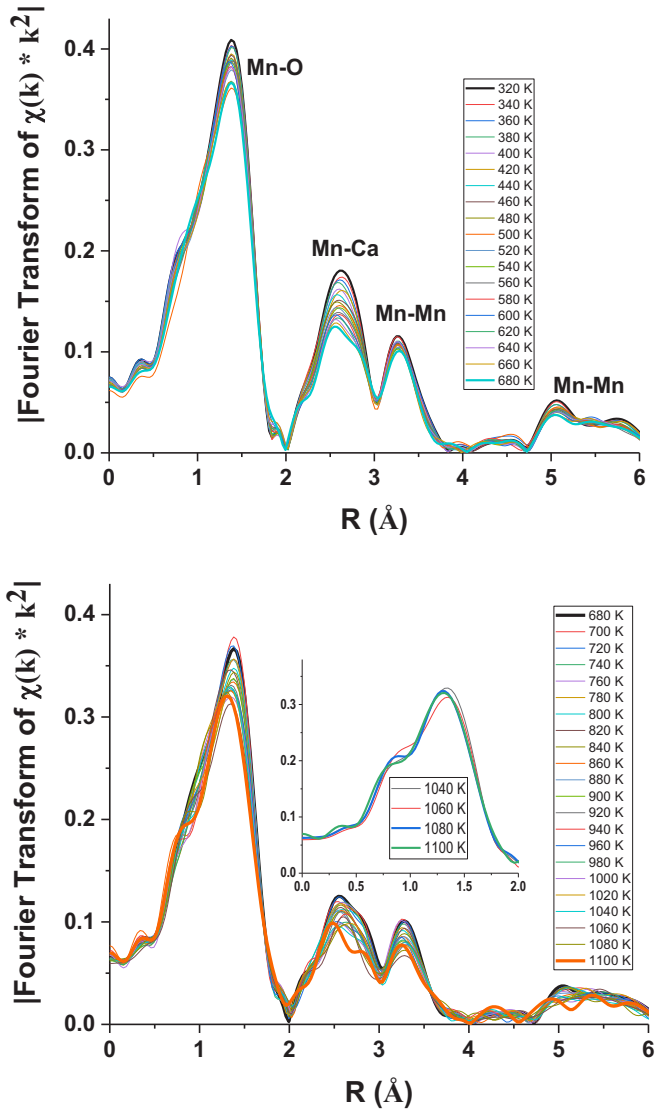


FIG. 4. XAFS structure function of $Ca_3Mn_2O_7$ measured between 320 and 1100 K [in (a) and (b)] revealing that the Mn-Mn first and second nearest neighbor in-plane correlations persist for the full temperature range. In (b) the inset shows that there is an abrupt reduction of the position of the Mn-O peak near 1060 K indicating the transition to the *I*4/*mmm* high symmetry structure.

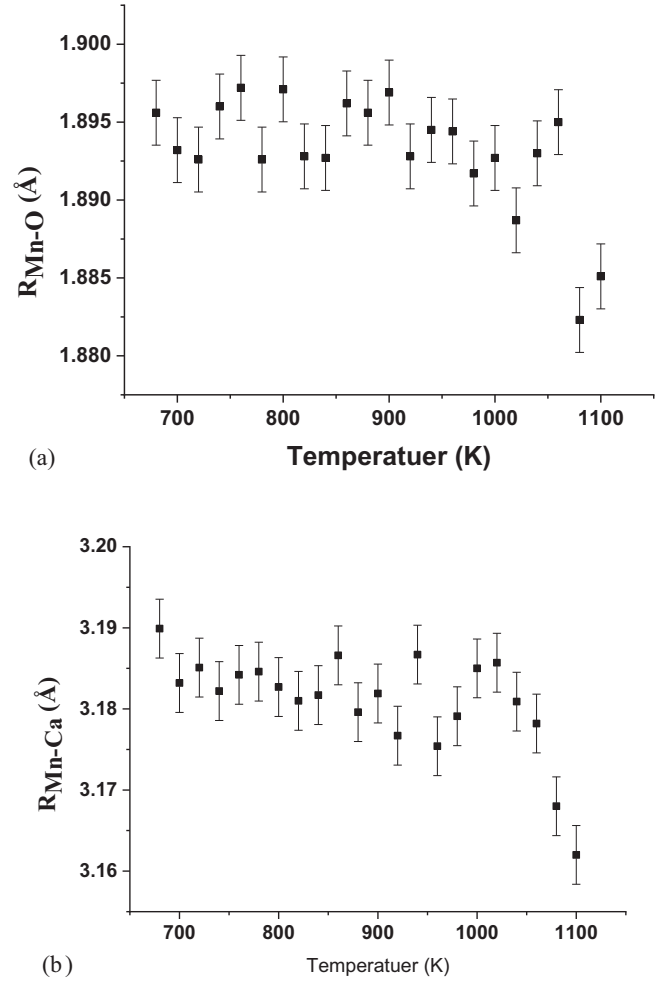


FIG. 5. Local structure results derived from XAFS measurements. In the high-temperature region, the (a) Mn-O and (b) Mn-Ca bond lengths reveal abrupt changes near 1060 K.

occur in the Ca-Mn correlation peak between 300 and 600 K. The Mn lattice sites are seen to form a very rigid network with major changes corresponding to the angular motion of rigid $MnO_6$ polyhedra units and the Ca ions. In the temperature region between 300 and 700 K (Fig. S12), an enhancement of the Mn-O peak width is seen near 400 K on warming.

Examination of the Ca site (Ca-O, Ca-Mn, and Ca-Ca bonds up to ∼4 Å) near the vicinity of the transition at 400 K reveal an enhancement of the Ca-Mn correlation (peak width of Ca-Mn distribution) on heating through $T_R$ indicating an increase on local symmetry at this transition. This can be seen in Figs. S13 and Table S2, where the Gaussian width of the Ca-Mn are found to become narrow on going above the $T_R$.

To follow the local structure trends in the $X$ = Ti system, Ti $K$-edge x-ray absorption near edge spectra (XANES) of crystal derived $Ca_{2.4}Sr_{0.6}Ti_2O_7$ samples were measured for temperatures between 300 and 540 K [Fig. S14(a)]. It was found that the main pre-edge feature [feature B in Fig S14(b)] increases in intensity with increasing temperature. Simulated

TABLE I. $Ca_3Mn_2O_7$ Self-force constants. For $Ca_3Mn_2O_7$ $U$ = 8.0 eV and $J$ = 0.88 eV (see Supplemental Material [12]).

| Ion Site | $k_x$ (long axis) (eV/Å$^2$) | $k_y$ (eV/Å$^2$) | $k_z$ (eV/Å$^2$) |
|---|---|---|---|
| $Ca_3Mn_2O_7$ (1 × 2 × 2) cell | | | |
| Mn | 25 | 25 | 25 |
| Ca1 | 8.2 | 8.3 | 8.0 |
| Ca2 | 12 | 8.0 | 7.3 |
| O1 (apical interior) | 20 | 9.3 | 6.3 |
| O2 (apical) | 16 | 7.2 | 5.9 |
| O3 (planar) | 7.5 | 14 | 15 |
| O4 (planar) | 7.9 | 14 | 14 |

XANES spectra for perovskite systems [Fig. S14(b)] showed that the reduction of tilting amplitude relative to the long axis (called the *a* axis here) increases the amplitude of peak B while reduction of twisting about the *z* axis reduces the peak amplitude (dotted line). Hence the observed continuous increase in the B feature amplitude for temperatures from 300 to 540 K is related to a continuous loss of tilt angle with increasing temperature above 300 K in $Ca_{2.4}Sr_{0.6}Ti_2O_7$. Hence, like the $Ca_3Mn_2O_7$ system, the $Ca_{2.4}Sr_{0.6}Ti_2O_7$ (representing $X$ = Ti) system shows a reduction in tilt angle with increasing temperature.

## V. NANOSCALE STRUCTURAL MEASUREMENTS (X-RAY PAIR DISTRIBUTION FUNCTION ANALYSIS)

More detailed structural information on $Ca_3Mn_2O_7$ and $Ca_3Ti_2O_7$ type systems was obtained on an intermediate length scale by PDF measurements between 100 and 1100 K [in real space fits over the range 1.3–20 Å (Fig. S15), single crystal based materials]. To determine the space group in $Ca_3Mn_2O_7$ on this intermediate structural level on crossing the transition near 400 K ($T_T$), fits to unit cells with possible space groups suggested previously [5] were examined including the groups $Cmc2_1$ (#36), *Amm*2 (#38), *Amam* (#63), *Acam* (#64), and *Acaa* (#68). The $R_W$ parameter indicating the fit quality was compared over the temperature range 200 to 450 K for each space group [see Fig. S16(a)]. ($R_W = \{\frac{\sum_{i=1}^{N} w(r_i)[G_{Obs}(r_i)-G_{Calc}(r_i)]^2}{\sum_{i=1}^{N} w(r_i)[G_{Obs}(r_i)]^2}\}$ was scaled by the number of independent parameters minus the number of free fittng parameters [14]). Additionally, comparisons of the space group $Cmc2_1$ (#36) with the nonpolar space group *I*4/mmm (#139) and $C2/m$ (#12, see below), both with cells having ½ the volume of the $Cmc2_1$ uint cell, were also conducted [Fig. S16(b)]. The results indicate that below ($T_T$), $Ca_3Mn_2O_7$ crystals possess $Cmc2_1$ space group symmetry on an intermediate structural range, while above it, the space group is closer to the $C2/m$ space group on this intermediate length scale (1.3–20 Å used in fits). Examining the *a*/*c* ratio (Fig. S17) reveals an abrupt transition near 400 K on warming and near 370 K on cooling consistent with the DSC measurements (Fig. 3). The high temperature PDF measurement over the range 300–1100 K (Fig. S18) reveals an abrupt change in $R_W$ near 1060 K and smooth increase in the *b*/*c* ratio at this transition but no change along the *c* axis consistent with rotation of the $MnO_6$ polyhedra ($T_R$).

In Fig. 6. we examine the change in the structure of $Ca_3Mn_2O_7$ on this length scale in more detail (with respect to the $Cmc2_1$ cell in Fig 1). In Fig. 6(a), the volume on cooling (3-K steps) reveals two distinct regions of thermal expansion behavior. The volumetric thermal expansion coefficient ($\alpha_V$) takes on the value $3.5(1) \times 10^{-5}\,K^{-1}$ above ~370 K and the value $2.63(4) \times 10^{-5}\,K^{-1}$ below it. Near 110 K evidence is seen for a negative thermal expansion corresponding to the onset of the magnetic ordering and spin lattice coupling. This corresponds to an anomoly in volume seen in polycrystalline $Ca_3Mn_2O_7$ samples [15]. The inset of the figure reveals hysteresis behavior covering the region between ~350 and ~400 K. [Consistent with earlier published work on polycrystalline samples [7], our PDF data on polycrystalline

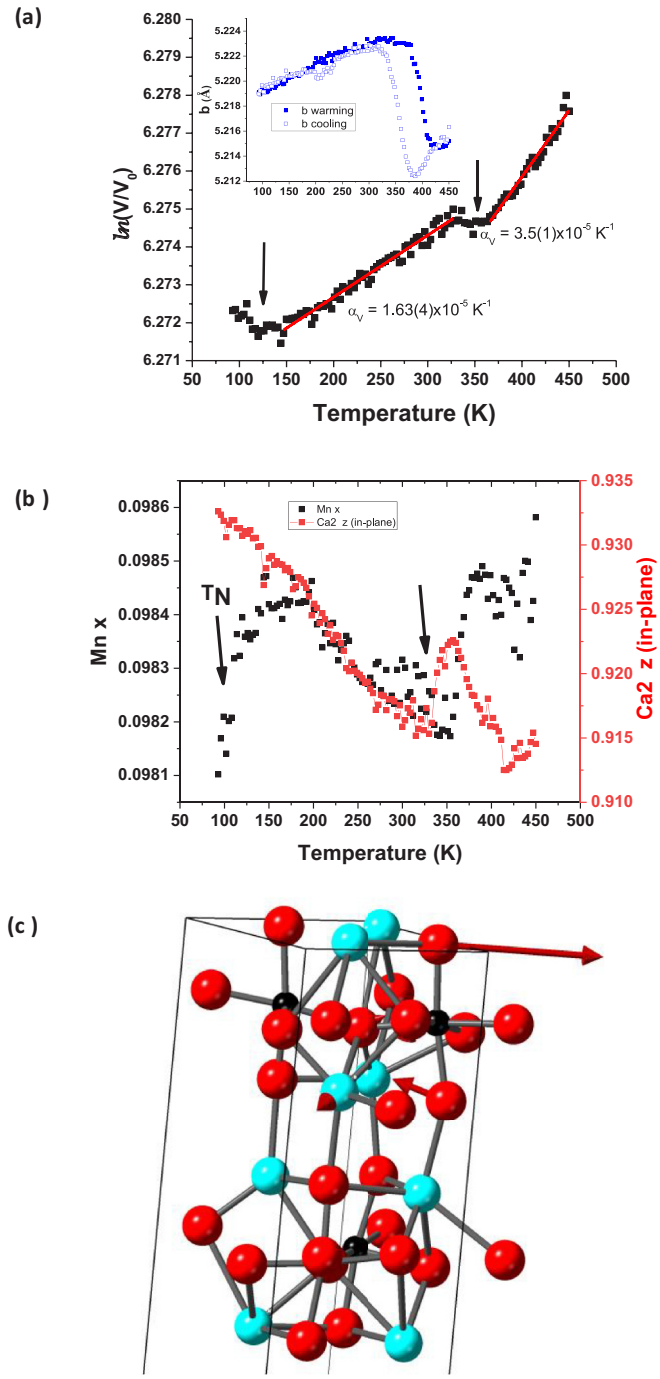


FIG. 6. Intermediate range structure results derived from PDF measurements. (a) Temperature-dependent volume (cooling data) with *b*-axis length shown as the inset (warming and cooling). Clear transitions are seen near ~350 K on cooling and near ~400 on warming (b-axis). The volume data also reveal a transition near 110 K, which is the magnetic ordering temperature (see also heat capacity data in Fig. S1). (b) Position (fractional coordinates) of the $Ca_2$ and Mn ions vs. temperature, revealing that only the Mn site position changes near 110 K and both Mn and Ca sites change near 370 K (cooling run). (c) Motion of ions going from 300 to 400 K. The arrows indicate a tilt rotation about an axis normal to the long axis.

samples (Fig. S19, inset) reveals hysteresis behavior covering a much broader region of temperature (∼250 to ∼400 K).] From Fig. 6(b), examination of the PDF *xyz* data (fractional coordinates) shows that the Mn *x* position changes abruptly at both $T_N$ and at $T_T$. However, the Ca *x* atomic position shows changes only at $T_T$. With the enhanced symmetry indicated by the XAFS results on the Ca local structure, this is consistent with a loss of polarization at $T_T$. The exact nature of the structural change was qualitatively determined by looking at the atomic displacements of the 400-K PDF structure relative to the structure at 300 K. In Fig 6(c), we see that the major displacements are for axial O atoms leading to reduction of the $MnO_6$ tilt amplitude ($X_3^-$ amplitude).

## VI. SINGLE CRYSTAL DIFFRACTION MEASUREMENTS (SPACE GROUP ABOVE $T_T$)

Accurate structural parameters of $Ca_3Mn_2O_7$ were derived from detailed synchrotron single crystal diffraction measurements on ∼20 $\mu$m diameter crystals between 300 and 480 K on warming. The low-temperature structure (104 K) was also determined. A high count rate Pilatus 1M detector ($10^7$ cps maximum/pixel) was utilized to obtain large signals for structure factors corresponding to scattering from both the light O atoms and heavy atoms (Mn/Ca). [Use of this detector with the high flux at a synchrotron beamline was found to enable the structural solution of atomic positions of *B* atoms in rare earth systems such as $HoAl_3$ $(BO_3)_4$ yielding accurate *B*-O distances (see Ref. [16]).] For each temperature data set, a systematic space group search was conducted [17–19]. Fits of full diffraction data sets to the $Cmc2_1$ structure were found to be stable for the temperature range 300 (fit parameter $R1 = 5.2\%$) to 380 K ($R1 = 5.6\%$). At 400 K the best structural refinements were obtained for the nonpolar spacegroups $I4/mmm$ ($R1 = 5.6\%$) and $C2/m$ ($R1 = 7.1\%$). Fits to the polar $Aba2$ space group at 400 K yielded $R1 = 10\%$ and large residual charge density. Measurements up to 480 K were taken, and the fits to $I4/mmm$ and $C2/m$ space groups yielded $R1 = 4.2\%$ and $R1 = 4.8\%$, respectively.

The full structural data from the refinements of $Ca_3Mn_2O_7$ at 480 K are given in Tables S3 and S4 for $I4/mmm$ and Table S5 for the $C2/m$ space group (both with cells ½ volume of the $Cmc2_1$ cell). The room temperature structural data ($Cmc2_1$) are given in Tables S6 and S7. Tables S4 and S7 and Fig. S21 can enable comparison of the bond distribution difference between the structures at 300 and 480 K. The room temperature results reproduce the previously published work [20]. Low-temperature data are given in Table S8 (104 K).

Using either of the high-temperature single crystal structure solutions ($I4/mmm$ or $C2/m$), it is found that the tilt angle in $Ca_3Mn_2O_7$ vanishes above $T_T$. Quantifying the result of Fig. 6(c), the $X_3^-$ tilt amplitude vanishes and hence, the electric polarization determined by the existence of both $X_3^-$ and $X_2^+$ distortion is predicted to vanish abruptly near 400 K on heating. The single crystal results are consistent with the abrupt in-plane shift at the Ca site seen in the PDF measurement. Figure 7 shows the 480 K structure ($I4/mmm$ space group), while the corresponding figure for the $C2/m$ space group is given in Fig. S20. Note that in both structural solutions the rotation amplitue ($X_2^+$) is nonzero at 480 K.

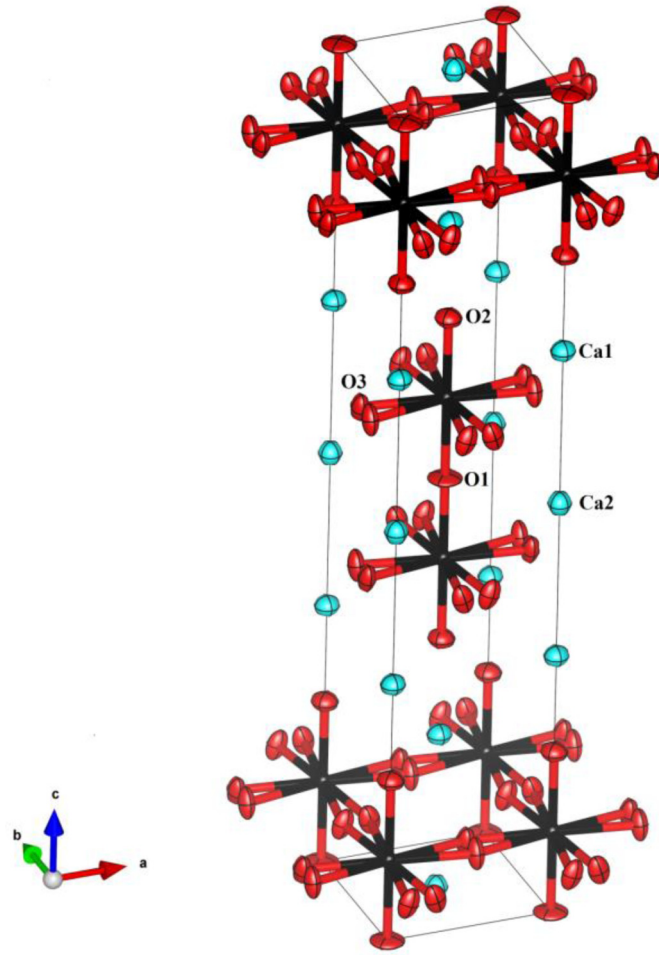


FIG. 7. Crystal structure at 480 K derived from single-crystal diffraction data ($I4/mmm$ space group). Note that the tilt angle vanishes. The planar oxygen atoms exist in two positions each with 50% probability indicating multiple domain structure but the rotation about the local *z* axis is nonzero relative to the cubic structure.

The in-plane O sites have double occupancy indicating the presence of 50/50 domains (by volume) with positive and negative in-plane rotations ($X_2^+$ mode) of the $MnO_6$ polyhedra but of the same magnitude (see structural results in Tables S3 and S5). It should be noted that the abrupt change in structure and loss of tilt seen in the single crystal measurements are consistent with first order behavior seen in the DSC and Raman measurements as well as with the abrupt changes in structure found in the PDF refinements. The electric polarization in $Ca_3Mn_2O_7$ is expected to vanish abruptly near $T_T$ while that in $Ca_3Ti_2O_7$ is expeceted to vanish continuously after passing through $T_T$.

## VII. HIGH-PRESSURE RAMAN MEASUREMENTS

To understand the softness of the tilting configuration in the $Ca_3Mn_2O_7$ system quantitatively, high-pressure Raman scattering measurements were conducted. In Fig. 8, data are shown for the pressure range 1 to 13.4 GPa for the same crystal orientation as in Fig. 3. The feature near 140 $cm^{-1}$, labeled A [Fig. 8(a)], is seen to vanish between 1.4 and

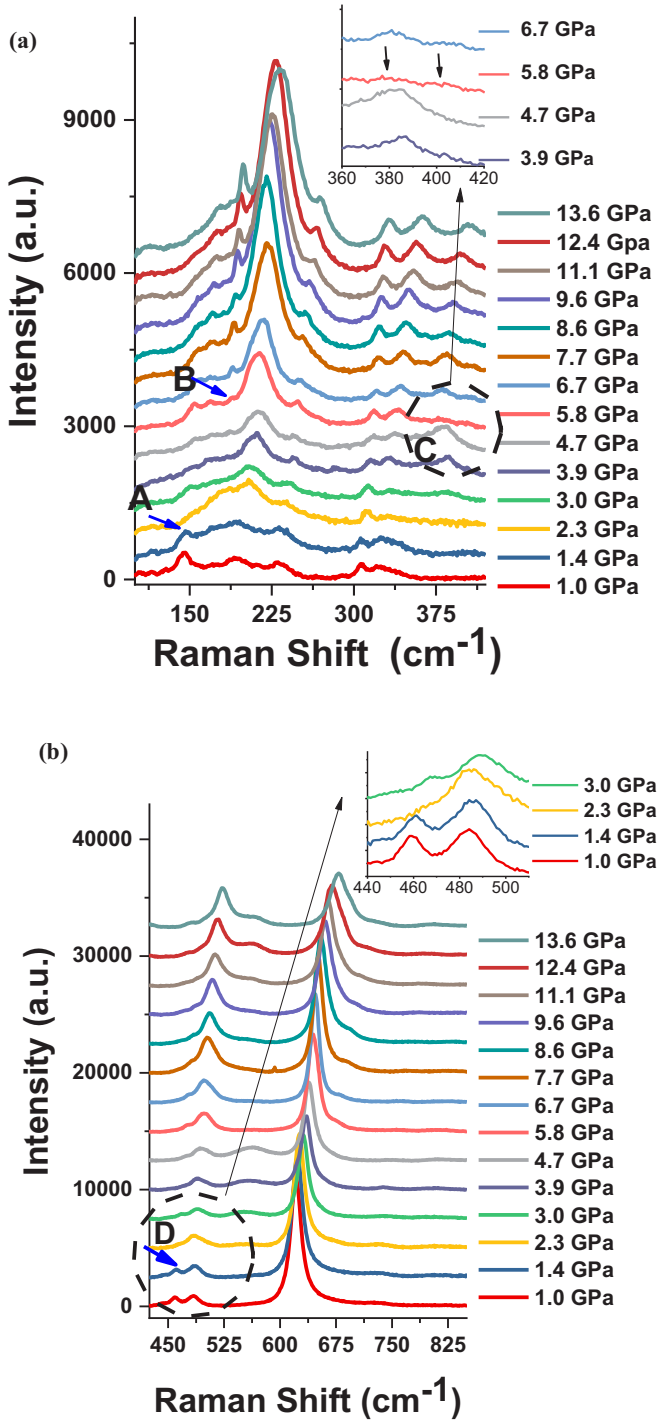


FIG. 8. High-pressure Raman measurements for the incident beam normal to (a) and parallel to (b) the long axis. High-pressure Raman data reveal a phase transition between 1.0 and 2.3 GPa observed as suppression of features A and D in panels (a) and (b). The feature D is expanded in the inset of panel (b). Panel (a) shows a second transition onsetting near 5.8 GPa as a new feature labeled B. This transition is also associated with the splitting of a peak near 380 $cm^{-1}$ indicated as feature C [inset to (a)].

2.3 GPa. In temperature-dependent ambient pressure Raman measurements (Fig. 2), this feature was associated with the loss of tilt and transition into a nonpolar phase as indicated by the combined structural and optical measurements. We find that at very low pressures, the system goes from the $Cmc2_1$ space group into a nonpolar space group ($C2/m$ or $I4/mmm$). Between 4.7 and 5.8 GPa [inset, Fig. 8(a)] the peak near 380 $cm^{-1}$ splits into two components and an additional feature near 190 $cm^{-1}$ onsets and grows larger as pressure rises (indicating symmetry reduction). Figure 8(b) and the corresponding inset again show the disappearance of the same feature between 1.4 and 2.3 GPa (near 460 $cm^{-1}$), which vanishes at $T_T$ in the ambient pressure data (Fig. 3).

## VIII. DISCUSSION OF COMBINED RESULTS

Development of an intuitive approach for the origin of the softness of the tilt mode is possible via simulations. The DFT derived self-force constants [21] (on-site terms in the force constant matrix, which indicates the force on the isolated atom with respect to unit displacements) are presented in Table I. For each unique site the directions are labeled by the unit cell in Fig. 1 (for both $Ca_3Mn_2O_7$ and $Ca_3Ti_2O_7$). The force constants of the Mn sites are seen to be approximately the same for displacements along the $a$, $b$, and $c$ axis for the Mn sites. They are also significantly larger than those of any other atomic sites. Combined with typically strong Mn-O bonds, the results predict rigid $MnO_6$ polyhedra as exemplified by the weak temperature dependence of the Mn-O XAFS peak (Fig. 4).

For the apical O sites, the force constants in the $yz$ plane are smaller than those for motion transverse to this plane ($k_y$, $k_z \sim 1/3\,k_x$ (long axis). The same holds for the apical interior O atoms. On the other hand, the planar (O3, O4) atoms have $k_y$, $k_z \sim 2\,k_x$. This predicts that local tilting [Fig. 1(b)] of the $MnO_6$ polyhedra corresponding mainly to $y/z$ displacement of the apical O and $x$ displacement of the planar O atoms will be softer than the rotation of the $MnO_6$ polyhedra about the $x$ axis (long axis). In the case of the rotation, the planar O atoms have $k_y$, $k_z \sim 2\,k_x$ making this type of distortion relatively stiffer. The same trend was found for self-force constants of the $Ca_3Ti_2O_7$ system. (The force constants do not change significantly with cell size and $U/J$ parameter change. See Table I and Supplemental Material Tables S9–S11.)

Previous work [5] predicted that tilt rotations would be the most stable, but this implies global tilting in all unit cells. What is observed experimentally is that the $X_3^-$ tilt amplitude vanishes while maintaining a finite $X_2^+$ rotation with increasing temperature in the $Ca_3X_2O_7$ system. The relative values of the force constants suggest that tilting is a softer distortion if produced on a short length scale. Combining these results, it is predicted that local tilting of single $MnO_6$ polyhedron in the lattice, as opposed to coherent long-range tilting of all $MnO_6$ polyhedra is a lower energy distortion than local rotation in both $Ca_3Mn_2O_7$ and $Ca_3Ti_2O_7$. By this we mean that there may be local domains with distinct tilting of the $MnO_6$ polyhedra. Also, in contrast with the current work, Ref. [11] suggests a difference in behavior between $Ca_3Mn_2O_7$ and $Ca_3Ti_2O_7$ with enhancement of both antiphase tilt and in-plane rotation occurring with increasing temperature in $Ca_3Ti_2O_7$; this is not observed in this work.

In addition to the possibility of local tilt or local rotation structural phases being the cause of the observed order of the transitions, we note that the relative stability of the $X_3^-$ and $X_2^+$

distortions is reversed by compressive biaxial strain of ∼1.5% [5] compared to the strain free or tensile strained systems. This strain value is at the level of accuracy for the determination of lattice parameters found in standard DFT simulations. It would be useful to explore more accurate methods than DFT+U to determine the stable structural phases.

## IX. SUMMARY

We note that the $Ca_3Mn_2O_7$ and $Ca_3Ti_2O_7$ exhibit a transition near 400 K with verified loss of inversion center in the case of $Ca_3Mn_2O_7$ (for temperatures below ∼400 K). The characteristic feature in these systems is the low energy local tilting of the Mn/Ti-$O_6$ polyhedra groups. To sustain the electric polarization at higher temperatures, it is necessary to strengthen the bonds on the Ca site (*A* site) in these systems. We also note that the low isotropic pressure needed to suppress the polarization state (1–2 GPa) will be significantly reduced if uniaxial pressure is applied. This may make it possible to switch the electric polarization on and off by depositing this material as a thin film on a piezoelectric substrate for films strained just below this critical strain value. The measurements also suggest that simulations beyond standard LDA+U may be needed to determine the ordering of the energetics of the distortions.

## ACKNOWLEDGMENTS

This work is supported by the National Science Foundation (NSF) Grant No. DMR-1809931. Work at Rutgers University is supported by the U. S. Department of Energy (DOE) Grant No. DE-GF02-07ER46382. This research used beamlines 8-ID, 22-IR-1, and 28-ID-2 of the National Synchrotron Light Source II, a U.S. DOE Office of Science User Facility operated for the DOE Office of Science by Brookhaven National Laboratory under Contract No. DE-SC0012704. Single crystal x-ray diffraction measurements were performed at NSF's ChemMatCARS Sector 15, which is principally supported by the NSF/DOE No. NSF/CHE-1834750. Beamline 22-IR-1 is supported by COMPRES, the Consortium for Materials Properties Research in Earth Sciences under NSF Cooperative Agreement EAR 1606856 and the DOE/NNSA (DE-NA-0003858, CDAC). Use of the Advanced Photon Source was supported by the U.S. DOE, Office of Science, Office of Basic Energy Sciences, under Contract No. DE-AC02-06CH11357. The Physical Properties Measurements System was acquired under NSF MRI Grant No. DMR-0923032 (ARRA award). This research used resources of the National Energy Research Scientific Computing Center, a DOE Office of Science User Facility supported by the Office of Science of the U.S. DOE under Contract No. DE-AC02-05CH11231. We are indebted to Prof. E. A. Nowadnick of NJIT for critical discussions and advice on simulations and central experiments.

[1] S. Picozzia and A. Stroppa, Eur. Phys. J. B **85**, 240 (2012).
[2] M. Okuyama and Y. Ishibashi, *Ferroelectric Thin Films: Basic Properties and Device Physics for Memory Applications* (Springer, Berlin, 2005).
[3] M. Dawber, K. M. Rabe, and J. F. Scott, Rev. Mod. Phys. **77**, 1083 (2005).
[4] M. T. Dove, Am. Mineral. **82**, 213 (1997).
[5] N. A. Benedek and C. J. Fennie, Phys. Rev. Lett. **106**, 107204 (2011).
[6] A. B. Harris, Phys. Rev. B **84**, 064116 (2011).
[7] M. S. Senn, A. Bombardi, C. A. Murray, C. Vecchini, A. Scherillo. X. Luo, and S. W. Cheong, Phys. Rev. Lett. **114**, 035701 (2015).
[8] B. Gao *et al.*, Appl. Phys. Lett. **110**, 222906 (2017).
[9] Y. S. Oh, X. Luo, F.-T. Huang, Y. Wang, and S.-W. Cheong, Nat. Mater. **14**, 407 (2015).
[10] A. Galmazda, D. Wulfreding, P. Lemmens, B. Gao, S.-W. Cheong, and K.-Y. Choi, Phys. Rev. B **97**, 094104 (2018).
[11] F. Ye, J. Wang, J. Seng, C. Hoffmann, T. Gu, H. J. Xiang, W. Tian, J. J. Molaison, A. M. dos Santos, M. Matsuda, B. C. Chakoumakos, J. A. Fernandez-Baca, X. M. Tong, B. Gao, J. W. Kim, and S.-W. Cheong, Phys. Rev. B **97**, 041112(R) (2018).
[12] See Supplemental Material at http://link.aps.org/supplemental/10.1103/PhysRevB.99.224105 for experimental details, additional measurements, and analysis for $X$ = Mn and full results for $X$ = Ti (see also Refs. [8,9,22–44]).
[13] L.-F. Huang, X.-Z. Lu, and J. M. Rondinelli, Phys. Rev. Lett. **117**, 115901 (2016).
[14] T. Egami and S. L. J. Billinge, *Underneath the Bragg Peaks: Structural Analysis of Complex Materials* (Pergamon, Amsterdam, 2003), p. 232.
[15] P. Sahlot, G. Sharma, V. G. Sathe, A. K. Sinha, and A. M. Awasthi, arXiv:1903.05995.
[16] H. Zhang, S. Liu, C. Nelson, L.N. Bezmaternykh, Y.-S. Chen, S. G. Wang, R. P. S. M. Lobo, K. Page, M. Matsuda, D. M. Pajerowski, T. J. Williams, and T. A. Tyson, Phys. Rev. B (to be published).
[17] Systematic space group searches were conducted using the integrated methods in SHELXT and PLATON.
[18] G. M. Sheldrick, Acta Cryst **A 71**, 3 (2015).
[19] A. L. Spek, Acta Crystallogr. **D 65**, 148 (2009).
[20] N. Guiblin, D. Grebille, H. Leligny, and C. Martin, Acta Crystallogr. **C 58**, i3 (2001).
[21] Ph. Ghosez, E. Cockayne, U. V. Wagjmare, and K. M. Rabe, Phys. Rev. B **60**, 836 (1999).
[22] A. Dewaele, M. Torrent, P. Loubeyre, and M. Mezouar, Phys. Rev. B **78**, 104102 (2008).
[23] H. K. Mao, J. Xu, and P. M. Bel, J. Geophys. Res. **91**, 4673 (1986).
[24] http://millenia.cars.aps.anl.gov/gsecars/ruby/ruby.htm.
[25] Y. Akahama and H. Kawamura, J. Appl. Phys. **100**, 043516 (2006).
[26] O. V. Dolomanov, L. J. Bourhis, R. J. Gildea, J. A. C. Howard, and H. Puschmann, J. Appl. Cryst. **42**, 339 (2009).
[27] G. Kresse and D. Joubert, Phys. Rev. B **59**, 1758 (1999).
[28] S. L. Dudarev, G. A. Botton, S. Y. Savrasov, C. J. Humphreys, and A. P. Sutton, Phys. Rev. B **57**, 1505 (1998).
[29] A. I. Liechtenstein, V. I. Anisimov, and J. Zaane, Phys. Rev. B **52**, R5467 (1995).
[30] A. Togo and I. Tanaka, Scr. Mater. **108**, 1 (2015).
[31] L. Chaput, A. Togo, I. Tanaka, and G. Hug, Phys. Rev. B **84**, 094302 (2011).

[32] T. A. Tyson, M. Deleon, S. Yoong, and S. W. Cheong, Phys. Rev. B **75**, 174413 (2007).
[33] B. Ravel and M. Newville, J. Synchrotron Rad. **12**, 537 (2005).
[34] *X-Ray Absorption: Principles, Applications, Techniques of EXAFS, SEXAFS and XANES*, edited by D. C. Konningsberger and R. Prins (Wiley, New York, 1988).
[35] K.V. Klementev, J. Phys. D **34**, 209 (2001).
[36] T. A. Tyson, T. Wu, K. H. Ahn, S.-B. Kim, and S.-W. Cheong, Phys. Rev. B **81**, 054101 (2010).
[37] Q. Qian, T. A. Tyson, C.-C. Kao, M. Croft, S.-W. Cheong, G. Popov, and M. Greenblatt, Phys. Rev. B **64**, 024430 (2001).
[38] T. A. Tyson (unpublished).
[39] T. A. Tyson, Phys. Rev. B **49**, 12578 (1994).
[40] R. B. Neder and Th. Proffen, *Diffuse Scattering and Defect Structure Simulations* (Oxford University, Oxford, 2008).
[41] T. Egami and S. L. J. Billinge, *Underneath the Bragg Peaks: Structural Analysis of Complex Materials* (Pergamon, Amsterdam, 2003).
[42] Th. Proffen, S. J. L. Billinge, T. Egami, and D. Louca, Z. Kristallogr **218**, 132 (2003).
[43] V. Petkov, *Characterization of Materials* (Wiley, Hoboken, NJ, 2012).
[44] P. Juhás, C. L. Farrow, X. Yang, K. R. Knox, and S. J. L. Billinge, Acta Crystallogr. A **71**, 562 (2015).